Molecular Biology of the Cell
Vol. 19, 3369–3378, August 2008

Aquaporin-4 Dynamics in Orthogonal Arrays in Live Cells Visualized by Quantum Dot Single Particle Tracking

Jonathan M. Crane,* Alfred N. Van Hoek,† William R. Skach,‡ and A. S. Verkman*

*Departments of Medicine and Physiology, Cardiovascular Research Institute, University of California, San Francisco, CA 94143-0521; †Center for Systems Biology, Program in Membrane Biology and Division of Nephrology, Massachusetts General Hospital, Boston, MA 02114; and ‡Department of Biochemistry and Molecular Biology, Oregon Health and Science University, Portland, OR 97239

Submitted March 28, 2008; Revised April 24, 2008; Accepted May 9, 2008
Monitoring Editor: Jennifer Lippincott-Schwartz

Freeze-fracture electron microscopy (FFEM) indicates that aquaporin-4 (AQP4) water channels can assemble in cell plasma membranes in orthogonal arrays of particles (OAPs). We investigated the determinants and dynamics of AQP4 assembly in OAPs by tracking single AQP4 molecules labeled with quantum dots at an engineered external epitope. In several transfected cell types, including primary astrocyte cultures, the long N-terminal "M1" form of AQP4 diffused freely, with diffusion coefficient $\sim 5 \times 10^{-10}$ cm^2/s, covering ~ 5 μm in 5 min. The short N-terminal "M23" form of AQP4, which by FFEM was found to form OAPs, was relatively immobile, moving only ~ 0.4 μm in 5 min. Actin modulation by latrunculin or jasplakinolide did not affect AQP4-M23 diffusion, but deletion of its C-terminal postsynaptic density 95/disc-large/zona occludens (PDZ) binding domain increased its range by approximately twofold over minutes. Biophysical analysis of short-range AQP4-M23 diffusion within OAPs indicated a spring-like potential, with a restoring force of ~ 6.5 pN/μm. These and additional experiments indicated that 1) AQP4-M1 and AQP4-M23 isoforms do not coassociate in OAPs; 2) OAPs can be imaged directly by total internal reflection fluorescence microscopy; and 3) OAPs are relatively fixed, noninterconvertible assemblies that do not require cytoskeletal or PDZ-mediated interactions for formation. Our measurements are the first to visualize OAPs in live cells.

INTRODUCTION

Aquaporin-4 (AQP4) is a water-selective plasma membrane transport protein expressed in glial cells, where it is involved in brain water balance, glial cell migration, and neural signal transduction (for review, see Verkman *et al*., 2006). AQP4 was cloned initially from lung (Hasegawa *et al*., 1994), and subsequently from brain, where two distinct isoforms were identified with different translation initiation sites (Jung *et al*., 1994; Yang *et al*., 1995; Lu *et al*., 1996). In immunoblot assays of rat cerebellum, the longer "M1" form of AQP4 (AQP4-M1) is visible as a 34-kDa band, whereas the shorter "M23" form of AQP4 (AQP4-M23) is visible as a 32-kDa band (Lu *et al*., 1996). Both isoforms of AQP4 function as water channels (Jung *et al*., 1994) and form stable tetramers, possibly heterotetramers. The relative abundances of AQP4 isoforms are tissue specific, with rat brain containing an approximate 3:1 ratio of AQP4-M23 to AQP4-M1 (Neely *et al*., 1999).

Our laboratory discovered that AQP4 is the protein responsible for formation of orthogonal arrays of particles (OAPs). OAPs are cobblestone-like square arrays of intramembrane particles that have been seen by freeze-fracture electron microscopy (FFEM) for >30 years in cell plasma membranes in brain and other tissues (Landis and Reese, 1974; Rash *et al*., 1974; Hatton and Ellisman, 1982). We first speculated that AQP4 may be the OAP protein based on its expression in the same cell types in which OAPs had been found (Frigeri *et al*., 1995). We identified characteristic OAPs in Chinese hamster ovary (CHO) cells after AQP4 transfection (Yang *et al*., 1996), and we demonstrated absence of OAPs in tissues from transgenic mice lacking AQP4 (Verbavatz *et al*., 1997). Label-fracture electron microscopy confirmed the presence of AQP4 in OAPs (Rash *et al*., 1998). FFEM in cells transfected with the AQP4-M1 versus AQP4-M23 showed that only the shorter form assembles into large OAPs of >100 particles, whereas AQP4-M1 tetramers are largely dispersed and form only occasional small arrays of <12 particles (Furman *et al*., 2003). Cotransfection of AQP4-M1 and AQP4-M23 showed a mixture of smaller OAPs (<100 particles) and dispersed particles, similar to what is observed in astrocyte endfeet (Furman *et al*., 2003; Silberstein *et al*., 2004). The biological relevance of AQP4 assembly into OAPs is not known, although it has been speculated that OAPs might enhance AQP4 water permeability (Yang *et al*., 1997; Van Hoek *et al*., 2000; Silberstein *et al*., 2004), maintain AQP4 polarization in astrocyte foot processes (Amiry-Moghaddam *et al*., 2004), and mediate cell–cell adhesion (Hiroaki *et al*., 2006). Correlations have been reported between OAP abundance and various disease processes such as toxic encephalopathies (Hatton and Ellisman, 1984) and muscular dystrophy (Schotland *et al*., 1981).

To date, FFEM has been the only approach to visualize OAPs, a method that cannot be used to study OAPs in live cells because it requires tissue fixation. The purpose of this study was to establish a simple, real-time approach to "im-

This article was published online ahead of print in *MBC in Press* (http://www.molbiolcell.org/cgi/doi/10.1091/mbc.E08–03–0322) on May 21, 2008.

Address correspondence to: Alan S. Verkman (alan.verkman@ucsf.edu).

age" OAPs in live cells to investigate their determinants and dynamics. We reasoned that AQP4 in large OAPs should be relatively immobile, whereas individual AQP4 tetramers or very small OAPs should be mobile. We used nanometer-resolution single particle tracking to follow AQP4 molecules labeled with quantum dots (Qdots) at an engineered external epitope, a strategy similar to that developed recently to demonstrate long-range, nonanomalous diffusion of AQP1 in cell membranes (Crane and Verkman, 2008). We found remarkable immobility of AQP4-M23 and rapid diffusion of AQP4-M1, and so exploited AQP4 diffusion as a "read-out" of OAP assembly in live cells to investigate a series of questions regarding the biophysics and determinants of OAP formation. We also developed a total internal reflection microscopy approach to visualize OAPs directly in fluorescently labeled fixed cells.

MATERIALS AND METHODS

DNA Constructs

To generate plasmid pSP64.AQP4M23.myc, which encodes rat AQP4 with a 10-residue c-myc epitope (Evan *et al*., 1985) inserted into the second extracellular loop (Hasegawa *et al*., 1994) between Val141 and Val142 (Figure 1A), the myc coding sequence (GAACAAAAGCTTATTTCTGAAGAAGATCTG) was introduced by polymerase chain reaction (PCR) overlap extension using as template plasmid pSP64.MIWC described previously (Shi *et al*., 1995). The resulting PCR fragment was digested with BlpI (base pair 85) and XbaI (base pair 903) and ligated into similarly digested pSP64.MIWC. The AQP4M23.myc sequence was subcloned into mammalian expression vector pcDNA3.1 at KpnI and EcoRI restriction sites. To generate AQP4M1.myc, a fragment from the M1 start codon to an internal HindIII restriction site in the c-myc-encoding sequence was PCR amplified using rat brain mRNA as template. The PCR product was digested with NheI and HindIII and ligated into similarly digested AQP4M23.myc. C-terminal deletion mutants of AQP4M23.myc (M23Δ6.myc) and AQP4M1.myc (M1Δ6.myc) were constructed by introducing TGA stop codons at base pair 886 by PCR using AQP4M1.myc as template, and then they were ligated into pcDNA3.1 at KpnI and EcoRI sites. All constructs were verified by sequence analysis. The construct for c-myc–labeled AQP1 (AQP1.T120.myc) was used as described previously (Crane and Verkman, 2008).

Cell Culture and Transfections

Primary cultures of astrocytes from neocortex of wild type and AQP4 null mice (Ma *et al*., 1997) were generated and grown as described previously (Saadoun *et al*., 2005). Cell lines included COS-7 cells (ATCC CRL-1651), Madin-Darby canine kidney (MDCK) type II cells (European Collection of Cell Cultures 00062107), CHO-K1 cells (ATCC CCL-61), and CHO-M23 cells (Yang *et al*., 1996). Cell cultures were maintained at 37°C in 5% CO_2, 95% air in appropriate medium containing 10% fetal bovine serum, 100 U/ml penicillin, and 100 μg/ml streptomycin. Six hours before transfections, cells were transferred to 12-well plates containing 18-mm-diameter glass coverslips by using antibiotic-free medium. Cells were transfected with Lipofectamine 2000 (Invitrogen, Carlsbad, CA) according to the manufacturer's protocol 24–48 h before experiments.

Labeling and Cell Treatments

Before labeling of AQP4 with Qdots, cells were washed with 3 ml of phosphate-buffered saline (PBS) containing 6 mM glucose and 1 mM pyruvate (GP buffer), and then they were incubated for 5 min in blocking buffer (GP buffer containing 1% bovine serum albumin), followed by 5 min with 70 ng/ml

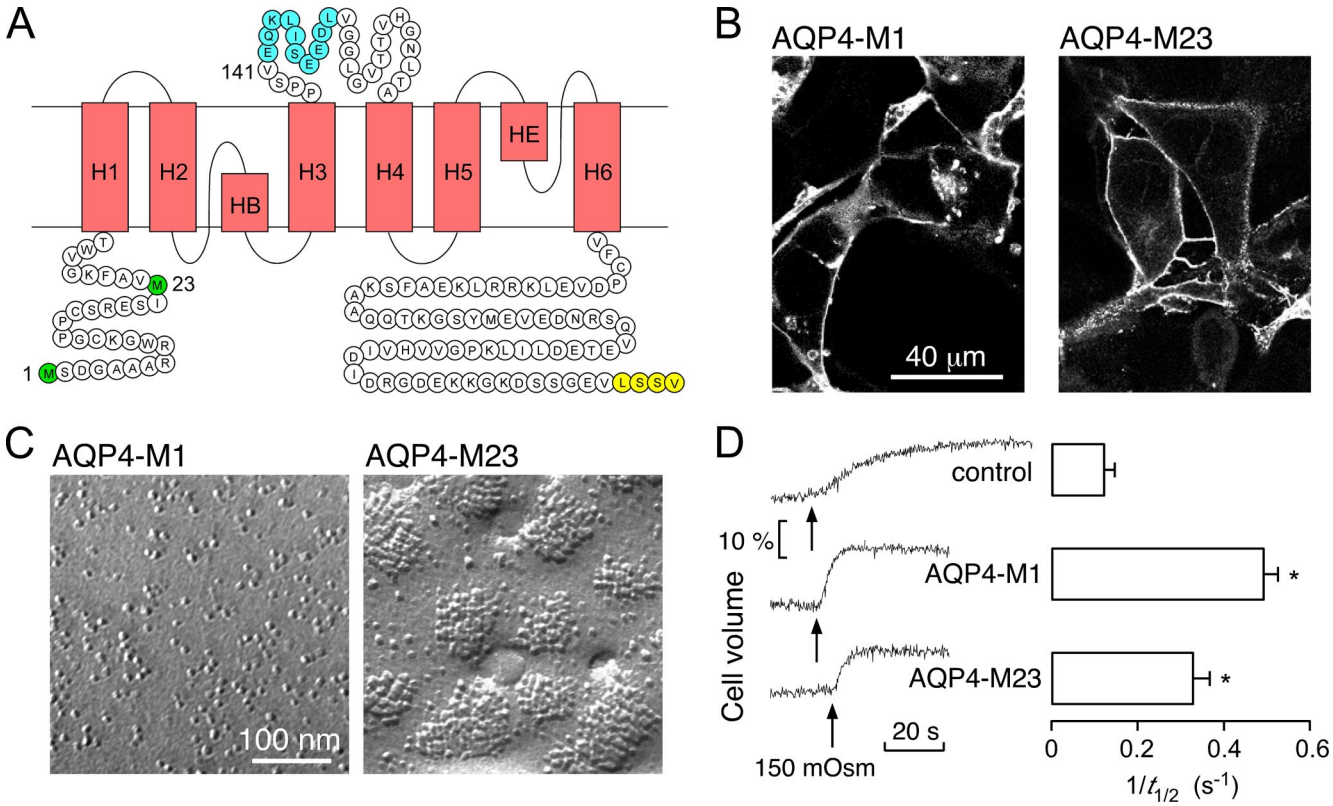

Figure 1. Characterization of cells expressing c-myc-tagged AQP4. (A) AQP4 schematic showing the positions of Met1 and Met23 (green) in the cytoplasmic N-terminal domain, the inserted c-myc sequence (blue) in the second extracellular loop, and the C-terminal PDZ binding domain (yellow). (B) Confocal micrographs of COS-7 cells transfected with c-myc–tagged AQP4-M1 (left) or AQP4-M23 (right) and labeled with Alexa555. (C) Freeze-fracture electron micrographs of the plasma membrane P-face of COS-7 cells expressing c-myc-tagged AQP4-M1 (left) or AQP4-M23 (right). (D) Osmotic water permeability measurements showing kinetics of osmotically induced cell volume changes (left) and fitted exponential time constants (right) for control COS-7 cells (top) versus cells expressing c-myc–tagged AQP4-M1 (middle) or AQP4-M23 (bottom) (mean ± SE, *$p < 0.01$ comparing to untransfected cells). Cell cytoplasm was stained with calcein and osmotic volume changed by switching the bathing solution from PBS (300 mOsm) to PBS diluted 1:1 with water (150 mOsm).

mouse anti-c-myc antibody (Covance, Emeryville, CA) in blocking buffer. Cells were then rinsed five times with GP buffer, incubated for 5 min with 0.1 nM goat F(ab′)$_2$ anti-mouse immumoglobulin G (IgG)-conjugated Qdot 655 (Invitrogen) in blocking buffer, then rinsed again 5 times with GP buffer. Coverslips were transferred to a custom-built perfusion chamber and maintained in GP buffer throughout the experiment.

For disruption of the cytoskeleton, cells were incubated with 0.5 μM latrunculin B (Invitrogen) or 10 μM nocodazole (Sigma, St. Louis, MO) in GP buffer at 37°C for 30 min before labeling. For stabilization of the actin skeleton, cells were incubated with 2.5 μM jasplakinolide (Sigma) for 10 min before labeling. Cytoskeletal modulators were also included in the labeling and experimental bathing solutions. In some studies, cells were fixed just after labeling by 10 min incubation with PBS containing 4% paraformaldehyde.

For heavy fluorescence labeling used in confocal and total internal reflection fluorescence microscopy (TIRFM), cells were fixed for 10 min with 4% paraformaldehyde, then rinsed with PBS. Fixed cells were incubated for 30 min in blocking buffer, then for 1 h with 7 μg/ml anti-c-myc in blocking buffer. Cells were again rinsed with PBS and incubated for 1 h with 10 μg/ml goat F(ab′)$_2$ anti-mouse IgG-conjugated Alexa Fluor 555 (Alexa555; Invitrogen) in blocking buffer. Cells were then rinsed extensively in PBS, and coverslips were mounted with VectaMount hard-set medium for microscopy (Vector Laboratories, Burlingame, CA).

Microscopy Instrumentation and Measurements

Single particle tracking (SPT) and imaging of green fluorescent protein (GFP)-labeled, Qdot-labeled, and calcein-loaded cells was performed on a Nikon Eclipse TE2000S inverted epifluorescence microscope (Nikon, Melville, NY) equipped with a Nikon 100× TIRF oil immersion objective (numerical aperture 1.45) and a deep-cooled charge-coupled device (CCD) camera (Hamamatsu EM-CCD; Hamamatsu, Bridgewater, NJ), giving a resolution of 80 nm/pixel. Qdot fluorescence was excited using a 420/40× excitation filter and 470DCXR dichroic mirror, and it was detected through a 655/40m emission filter (Chroma Technology, Rockingham, VT). GFP and calcein fluorescence was excited and detected using filter set 31001 (Chroma Technology). Data were obtained at 37°C within 30 min of the final wash step after cell labeling. "Long-range" SPT was done using time-lapse image acquisition in which 100-ms exposures were acquired at a rate of 1 Hz for 6 min, with the illumination light shuttered between exposures. "Short-range" SPT was done using continuous 11-ms acquisitions for 6 s (91 Hz). The spatial resolution of the system, determined from the SD of x,y-coordinates of immobilized Qdots on a coverglass (Fujiwara *et al*., 2002), was 18 nm at 91 Hz. In most cells, Qdots could be tracked on both the apical and adherent cell membranes, with no difference in diffusion observed between the two surfaces. In MDCK cells, only Qdots on the apical membrane were measured.

TIRFM was done using a Nikon Eclipse TE2000E microscope with a through-objective TIRF attachment and a 100× TIRF oil immersion objective (numerical aperture 1.49) mounted on a perfect focus module (Nikon). An argon-ion laser (Spectra Physics, Mountain View, CA) on a custom-built launch was coupled through a fiber-optic to the TIRF module. Alexa555-labeled AQP4 was excited using a Z514/10× excitation filter and Z514RDC dichroic mirror, and it was detected through a 605/40m emission filter (Chroma Technology). Images were acquired by a QuantEM 512SC deep-cooled CCD camera (Photometrics, Tuscon, AZ). Confocal images were acquired with a Nikon EZ-C1si spectral confocal microscope with a 40× oil immersion objective.

SPT Analysis

Image sequences were analyzed and trajectories constructed using IDL software (Research Systems, Boulder, CO), with algorithms available as shareware at http://www.physics.emory.edu/~weeks/idl/. Blinking of individual Qdots was accounted for during trajectory constructions. Trajectories were considered to be continuous if a blinking Qdot was rediscovered within a four-pixel radius and 20-frame window. Trajectories were analyzed as described in detail previously (Jin *et al*., 2007; Crane and Verkman, 2008) to determine the mean squared displacement (MSD), diffusion coefficient, diffusion range, and diffusion type, as well as potentials for confined diffusion, by using custom programs written in LabVIEW (National Instruments, Austin, TX). The MSD as a function of time $\langle r^2(t)\rangle$ was constructed for each trajectory, and the diffusion coefficient D_{1-3} and offset due to noise was determined by a linear fit to the first three steps to the MSD:

$$\langle r^2(t)\rangle_{1-3} = 4D_{1-3}t + \text{offset} \quad (1)$$

The offset was subtracted from each point on the MSD versus t curve, and the first 25% of the curve (Saxton, 1997) was fitted using a weighted Levenberg–Marquardt nonlinear least-squares fitting algorithm to a combined quadratic, polynomial, and exponential function with fitting parameters a_1, a_2, $a_3 \geq 0$, such that $\langle r^2(t)\rangle_{\text{fit}} = a_1t^2 + a_2[1 - \exp(-a_3t)]$ (Haggie *et al*., 2006). The fit was weighted by the variance in the MSD at each time step. The range of an individual particle at specific time t was computed as follows:

$$\text{range}(t) = \langle r^2(t)\rangle_{\text{fit}}^{1/2} \quad (2)$$

The relative deviation (RD) (Kusumi *et al*., 1993) of the MSD from linearity, measured at the nth step of a trajectory with total length N, was defined as follows:

$$\text{RD}(N, n) = \frac{\langle r^2(n\delta t)\rangle_{\text{fit}}}{4D_0 n\delta t} \quad (3)$$

where δt is the temporal resolution of the acquisition and $4D_0$ is the initial slope of $\langle r^2(t)\rangle_{\text{fit}}$. Particles were identified as "free" or "restricted" based on the calculated RD at 50 frames and a statistical comparison to simulated free diffusion as described previously (Crane and Verkman, 2008). Immobile particles were defined as those with a range <18 nm (limit of positional accuracy) after 100 steps. Mean values of D_{1-3} were derived from mobile particles only. The potential function $V(r)$ acting on AQP4 in OAPs was determined by nonlinear least-squares regression to the radial particle density distribution $d(r)$ of trajectories exhibiting confined diffusion according to the Boltzman distribution:

$$d(r) = d(0)\exp(-V(r)/k_BT). \quad (4)$$

where r is the distance from the potential origin, k_B is the Boltzman constant, and T is absolute temperature (Jin *et al*., 2007).

Only trajectories >200 steps were analyzed by MSD, with data sets composed of at least 200 trajectories from at least 14 cells, from at least two independently labeled cell cultures. Only trajectories longer than 5 s (455 frames) were used for calculation of confining potentials. Statistical significance of differences in mean values was determined using the Student's t test.

Water Permeability Measurements

After Qdot labeling AQP4 in transfected COS-7 cells, cells were loaded with calcein by incubation for 10 min in 10 μM calcein-AM (Invitrogen). Cells were then washed with PBS, and the coverslip was placed in a custom laminar-flow perfusion chamber designed for rapid solution exchange without causing cell detachment (Solenov *et al*., 2004). AQP4-positive cells were distinguished from control cells by Qdot fluorescence. Calcein fluorescence was recorded at 2 Hz as solutions were exchanged between normal PBS (300 mOsm) and hypotonic saline consisting of PBS diluted with distilled water (150 mOsm). For single cells in the microscopic field of view, two or more linear axes through the cell center were chosen for temporal analysis of fluorescence intensity profiles. Changes in cell width along each axis were calculated from changes in the distance between fluorescence half-maxima during cell swelling, and the $t_{1/2}$ of swelling was calculated by single exponential regression to width versus time data. Using this method, water permeability of control and AQP4-positive cells could be measured on a single coverslip. For comparison, coverslips of entirely nontransfected cells were also studied.

Freeze-Fracture Electron Microscopy

Transiently transfected COS-7 cells were checked for AQP4 expression by whole-cell immunostaining. Only populations with >60% transfection efficiency were chosen for FFEM. Cells were fixed with 2% glutaraldehype/0.1 M cacodylate (Electron Microscopy Sciences, Hatfield, PA) for 4 h, and then they were rinsed with 0.1 M cacodylate, followed by PBS. After cryoprotection for at least 1 h in 30% glycerol, cells were scraped from the culture dish, and clumps of cells were placed on a copper freeze-fracture support and frozen in Freon 22 cooled by liquid nitrogen. Freeze-fracture replicas from cells were produced as described previously (Silberstein *et al*., 2004). After removal from the freeze-fracture device, the replicas were cleaned by immersion for 2 h in concentrated sodium hypochlorite bleach. Replicas were washed three times for 5 min each with distilled water, picked up on copper electron microscopy grids, and examined with a JEOL 1011 electron microscope (JEOL, Tokyo, Japan). Images from E-face and P-face views were captured with a Hamamatsu digital camera interfaced by AMT Image Capture Engine software (Advanced Microscopy Techniques, Danvers, MA). OAP sizes were determined from measurements of length and width, or radius, in Adobe Photoshop (Adobe Systems, Mountain View, CA).

RESULTS

A c-myc epitope was engineered in the second extracellular loop of AQP4 monomers for Qdot labeling in live cells (Figure 1A). The location for epitope insertion was chosen following the success of a similarly labeled AQP1 construct for studies of AQP1 topology (Lu *et al*., 2000) and diffusion (Crane and Verkman, 2008).

Initial experiments were done to verify that the c-myc insertion did not affect AQP4 processing, function, or assembly in OAPs. Confocal fluorescence images of COS-7 cells heavily labeled with anti-c-myc primary antibody and Alexa555-conjugated secondary antibody showed fluorescence

of the short (M23) and long (M1) forms of AQP4 over the entire cell plasma membrane (Figure 1B). FFEM of COS-7 cells expressing c-myc-tagged AQP4-M23 showed characteristic intramembrane particles (IMPs) organized in large OAPs on the plasma membrane P-face (Figure 1C), similar to those observed in various other cell types expressing AQP4-M23 (Yang *et al.*, 1996; Rash *et al.*, 1998; Silberstein *et al.*, 2004). OAPs contained from 30 to 500 IMPs, with lattice spacing of 8.7 nm, consistent with one AQP4 tetramer per IMP. In contrast, intramembrane particles in cells expressing AQP4-M1 seemed to be randomly scattered in the membrane, with no OAPs seen. To verify AQP4 water transport function serial fluorescence images were acquired of calcein-stained cells following osmotic challenge. Cells expressing AQP4-M23 or AQP4-M1 showed three- to fourfold increased osmotic swelling rates compared with control, nontransfected cells (Figure 1D), confirming that both epitope-tagged AQP4 isoforms were functional water channels.

We first characterized the long-range motions of Qdot-labeled AQP4-M1 and AQP4-M23 in COS-7 cell membranes using time-lapse image acquisition at 1 Hz over 6 min. Cells were cotransfected with GFP to define their boundaries. Examples of Qdot trajectories are shown in Figure 2A (also see Supplemental Movie 1). Figure 2, C and D, show the combined MSD versus time plots for all measured trajectories, and Figure 2E shows the cumulative distribution of ranges at 1 min (Eq. 2). Most AQP4-M1 molecules diffused freely over the entire cell membrane, with an average range of 1.7 ± 0.4 μm in 1 min (SD, 516 trajectories; 14 cells), and up to 15 μm in 5 min. In contrast, AQP4-M23 diffusion was limited to an average range of 0.13 ± 0.03 μm in 1 min (534 trajectories; 16 cells). An overlay plot of the centroid positions all AQP4-M23 trajectories on one cell (with initial positions displaced to the origin) revealed a symmetrical distribution (Figure 2B); an overlay plot after paraformaldehyde fixation showed greatly reduced range. These results confirm that the observed AQP4-M23 movement is diffusive, and not due to cell migration, microscope stage drift, or inadequate *x,y*-spatial resolution.

AQP4 contains a C-terminal postsynaptic density 95/disc-large/zona occludens (PDZ) binding domain, Leu-Ser-Ser-Val (Figure 1A), which could be involved in intermolecular interactions related to AQP4 polarization or basolateral membrane targeting (Neely *et al.*, 2001). We therefore measured by time-lapse SPT the diffusion of a C-terminal deletion mutant of AQP4-M23 (M23Δ6). M23Δ6 diffused over an average range of 0.24 ± 0.05 μm in 1 min, approximately twofold greater than that of full-length AQP4-M23 (Figure 2, D and E), although much less than that for AQP4-M1, suggesting that PDZ domain deletion does not disrupt OAP formation but may interfere with AQP4 interactions involved in membrane anchoring. Close examination of M23Δ6 trajectories revealed occasional parallel diffusion of nearby Qdots (Figure 2F) (also see Supplemental Movie 2), indicating codiffusion of multiple AQP4 molecules within a large diffusing OAP.

To determine whether the apparent anchoring of AQP4-M23 OAPs involves cytoskeletal elements, time-lapse SPT measurements were done after chemical alteration of actin polymerization state and tubulin. Microtubule disruption by nocodazole did not affect AQP4-M23 diffusion (Figure 2, D and E). Depolymerization of actin by latrunculin B, or stabilization of filamentous actin by jasplakinolide, modestly reduced the slope of AQP4-M23 MSD curves (Figure 2D). Treatment with jasplakinolide produced a slight shift to lower diffusion of the entire population of AQP4-M23, with an average range of 0.10 ± 0.03 μm at 1 min, whereas latrunculin B produced a broadening of the distribution of AQP4-M23 diffusion with no significant change in the average range (Figure 2E and Table 1). These observations are explored further (see below) by SPT studies at high frame rates.

Although time-lapse SPT over minutes provided an overview of the long-range diffusion of AQP4 isoforms, quanti-

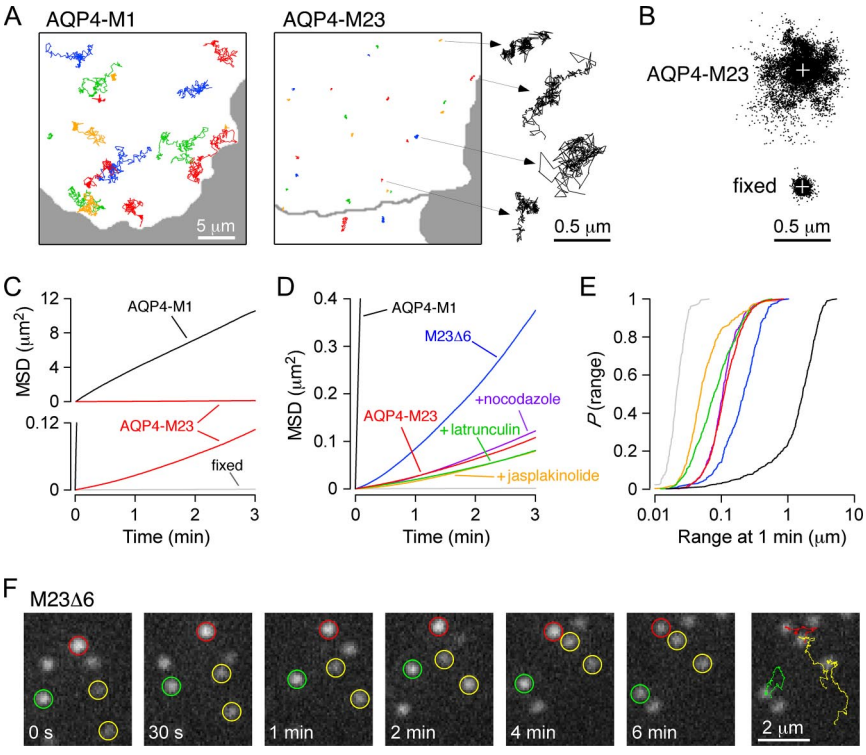

Figure 2. Time-lapse (long-range) single particle tracking of quantum dot-labeled AQP4 at 1 Hz for 6 min. (A) Representative trajectories superimposed on cellular profiles (white regions) of COS-7 cells expressing AQP4-M1 (left) or AQP4-M23 (right). Cells were cotransfected with GFP to identify cell boundaries. (B) Overlay dot-plot of *x* and *y* positions of AQP4-M23 trajectories in A, with initial particle positions displaced to the origin (top). Similar plot but after paraformaldehyde fixation (bottom). (C) Combined MSD versus time plots for AQP4-M1 (black) and AQP4-M23 (red). Expanded plot on the bottom also shows MSD for AQP4-M23 in fixed cells (gray). (D) Combined MSD versus time plots for AQP4-M1 (black), AQP4-M23 (red), and M23Δ6 (blue) in untreated COS-7 cells, and after treatment with latrunculin B (green), jasplakinolide (orange), nocodazole (purple) or paraformaldehyde (gray). (E) Cumulative distribution of ranges at 1 min for AQP4 in COS-7 cells, with colors same as in D. (F) Time image series showing codiffusing Qdots (yellow circles) in COS-7 cells expressing M23Δ6. Green and red circles show independently diffusing Qdots. Corresponding trajectories are shown at the far right.

Table 1. Summary of average diffusion coefficients and ranges for aquaporins in COS-7 cells

	D_{1-3} (cm^2/s)	Range at 1 s (μm)	Range at 1 min (μm)
AQP4-M1	$(5.2 \pm 2.2) \times 10^{-10}$	0.34 ± 0.09	1.7 ± 0.4
+latrunculin	$(7.2 \pm 2.9) \times 10^{-10}$	0.40 ± 0.10	—
+jasplakinolide	$(5.6 \pm 2.0) \times 10^{-10}$	0.34 ± 0.07	—
M1Δ6	$(7.1 \pm 1.9) \times 10^{-10}$	0.44 ± 0.09*	—
AQP4-M23	$(5.9 \pm 3.1) \times 10^{-11}$	0.040 ± 0.014	0.13 ± 0.03
+latrunculin	$(5.5 \pm 2.8) \times 10^{-11}$	0.049 ± 0.024	0.11 ± 0.07
+jasplakinolide	$(4.3 \pm 1.6) \times 10^{-11}$	0.031 ± 0.006*	0.10 ± 0.03
M23Δ6	$(6.9 \pm 3.6) \times 10^{-11}$	0.046 ± 0.012	0.24 ± 0.05*
AQP1	$(8.1 \pm 3.2) \times 10^{-10}$	0.46 ± 0.14	2.0 ± 0.4

Mean ± SD D_{1-3} (Equation 1) and range at 1 s (Equation 2) determined by SPT at 91 Hz. Range at 1 min determined by time-lapse SPT at 1 Hz. *$p < 0.01$ when compared to untreated AQP4.

tative biophysical analysis of diffusion coefficients and mechanisms requires acquisition at higher frame rates. Figure 3A shows trajectories of AQP4-M1 and AQP4-M23 acquired at 91 Hz over 6 s (also see Supplemental Movie 3). These data indicate that AQP4-M1 diffusion is largely Brownian, with an average diffusion coefficient D_{1-3} of ~5 × 10^{-10} cm^2/s and an average range of 0.34 ± 0.09 μm at 1 s (Table 1). The short-range diffusion of AQP4-M1 was qualitatively similar to its long-range diffusion in terms of rapid, free diffusion. However, the diffusion of AQP4-M23 over short times showed rapid, confined AQP4-M23 movements (within a slowly diffusing array), a phenomenon that cannot be seen in the slower time-lapse measurements. In most cases, AQP4-M23 diffusion over 6 s was restricted to a circular area, whereas occasionally a particle was observed "hopping" to a nearby location (Figure 3A, right), which may represent hopping of individual AQP4 tetramers within an array or between adjacent arrays. The combined MSD versus time plot for AQP4-M23 shows the characteristic negative curvature expected for confined or anomalous diffusion (Figure 3C), with the average diffusion coefficient and range at 1 s being an order of magnitude lower than that of AQP4-M1 (Figure 3B and Table 1). In addition to measuring the diffusion of the individual AQP4 isoforms, we measured diffusion in COS-7 cells cotransfected with AQP4-M1 and AQP4-M23. As shown in Figure 3B, the distribution of ranges at 1 s is bimodal. Label-fracture studies have shown previously that <5% of AQP4-M23 resides outside of OAPs in transfected cells (Furman *et al.*, 2003). We estimated (using as cutoff the 95th percentile of the range of AQP4-M23 diffusion) that ~45% of AQP4 was confined to arrays in the cotransfected cells. The average AQP4 diffusion coefficients below and above this cutoff range were nearly identical to those in cells expressing AQP4-M23 and AQP4-M1 individually; however, the average range at 1 s of the OAP-associated fraction from the cotransfected cells was ~10 nm greater than for AQP4-M23

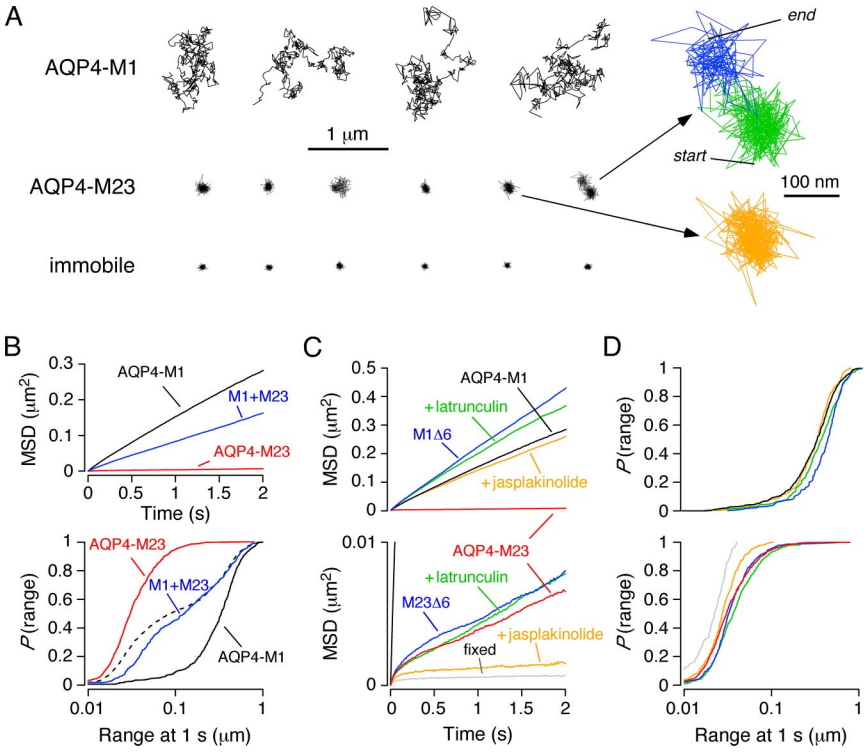

Figure 3. Single particle tracking of quantum dot-labeled AQP4 at 91 Hz for 6 s. (A) Representative trajectories of AQP4-M1 (top) and AQP4-M23 (middle), compared with immobilized Qdots on a coverglass (bottom). Examples of AQP4-M23 trajectories shown expanded on the right. Symmetric diffusion in a circular area generally seen (yellow), with Qdot hopping to an adjacent position (green and blue) occasionally seen. (B) MSD versus time plots (top) and cumulative distribution of ranges at 1s (bottom) of COS-7 cells expressing AQP4-M1 (black), AQP4-M23 (red), or both (blue). Dashed curve represents the prediction for an equal amount of AQP4-M1 and AQP4-M23. (C) Combined MSD versus time plots. Top, AQP4-M1 (black) and M1Δ6 (blue) in untreated COS-7 cells, and AQP4-M1 after treatment with latrunculin B (green) or jasplakinolide (orange). Bottom, AQP4-M23 (red) and M23Δ6 (blue) in untreated COS-7 cells, and AQP4-M23 after latrunculin B (green), jasplakinolide (orange), or paraformaldehyde (gray). (D) Cumulative distribution of ranges at 1 s for AQP4 in COS-7 cells, with colors same as in C.

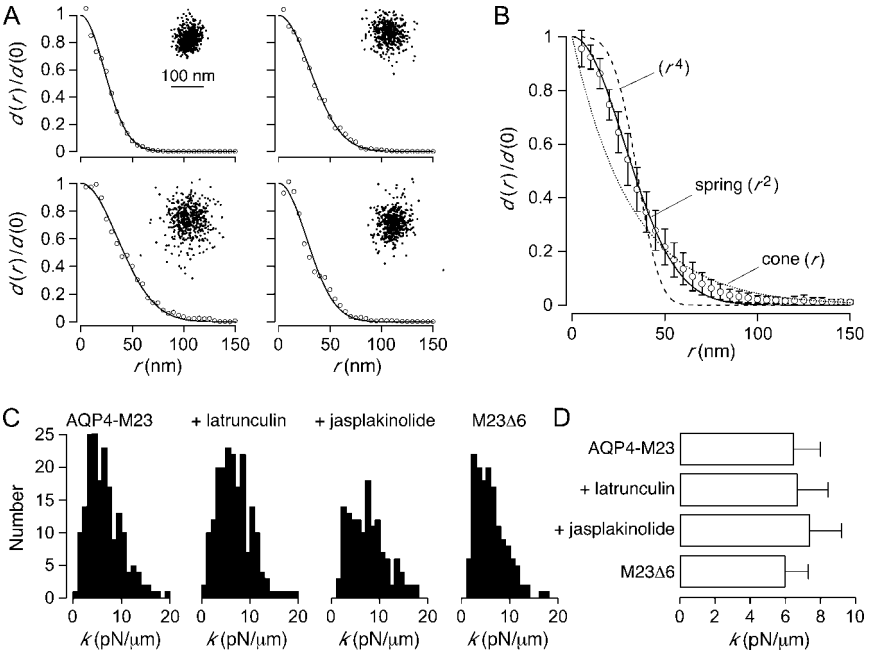

Figure 4. Confinement potentials $V(r)$ for diffusion of AQP4 in OAPs in COS-7 cells. (A) Particle positions and corresponding radial density function, $d(r)/d(0)$, for four representative AQP4-M23 trajectories. Solid lines represent best fits to $d(r)/d(0)$ for a spring potential, $V(r) \sim r^2$. (B) Mean $d(r)/d(0)$ from 215 AQP4-M23 trajectories (± SD) with best fits to indicated $V(r)$. (C) Histograms of spring constants k for AQP4-M23 in untreated COS-7 cells (left) and after treatment with latrunculin (middle left) or jasplakinolide (middle right), and M23Δ6 in untreated cells (right). (D) Average k (± SD) from distributions in C.

alone ($p < 0.01$) (Figure 3B), suggesting that the presence of AQP4-M1 mildly disrupts OAPs.

As mentioned above, we hypothesized that increased diffusion of AQP4-M23 seen in time-lapse SPT after deletion of its C-terminal PDZ binding domain was not due to OAP disruption, but to the disruption of OAP anchoring interaction(s). SPT at 91 Hz confirmed this hypothesis, because the short-range diffusion of M23Δ6 was nearly identical to that of full-length AQP4-M23. Deletion of the PDZ binding domain in AQP4-M1 (M1Δ6) resulted in a slight increase in diffusion, indicating that the diffusion of individual AQP4 tetramers is mildly slowed by PDZ interactions (Figure 3, C and D). Actin depolymerization by latrunculin B did not affect the short-range motions of AQP4-M23, but it produced a small increase in the diffusion of AQP4-M1. F-actin stabilization by jasplakinolide further reduced the confinement area of AQP4-M23, but it did not change the diffusion of AQP4-M1. These data suggest that the actin cytoskeleton interacts weakly with AQP4, but it is not involved in OAP stability.

To further characterize the biophysics of AQP4-M23 confinement in OAPs, we deduced from the spatial profiles of AQP4-M23 diffusion the energy potential (and consequent forces) confining individual AQP4-M23 molecules. Our laboratory recently developed an analysis method to deduce the potential function for confined particle diffusion, $V(r)$, from particle radial density distribution $d(r)$ (Jin *et al*., 2007). Radial density distributions for AQP4-M23 were fitted to models for diffusion in hard-wall, cone [$V(r) = V_0 r$], spring [$V(r) = V_0 r^2$], and $V(r) = V_0 r^4$ potentials, where V_0 is the potential strength (Eq. 4). Trajectories included in the analysis were at least 5 s in length and showed restricted diffusion by RD analysis. Of 215 AQP4-M23 trajectories meeting these criteria, ~90% fit best to a spring potential (four examples shown in Figure 4A). Figure 4C shows the distribution of the "restoring force" (spring constant) k values, with average values summarized in Figure 4D. The average k was 6.5 ± 1.5 pN/μm for AQP4-M23 diffusion in untreated cells, not significantly different from that after exposure to latrunculin or jasplakinolide, or after C-terminal PDZ binding domain deletion in M23Δ6. As mentioned above, an increased range at 1 s was found for the confined fraction of AQP4 in cells cotransfected with both M23 and M1 isoforms (Figure 3B). The density function for the confined fraction in the cotransfected system also fit best to a spring-like potential, with average k of 5.2 ± 2.3 pN/μm, slightly lower than that in OAPs in the pure AQP4-M23 system ($p < 0.02$).

To verify the generality of our findings on AQP4 diffusion in COS-7 cells, and to test further for coassembly of AQP4-M23 and AQP4-M1 in OAPs, we measured AQP4 diffusion in several cell types, including primary astrocyte cultures. As shown by MSD analysis (Figure 5A), large differences in the diffusion of AQP4-M1 versus AQP4-M23 were seen in each cell type. Average diffusion coefficients and ranges were an order of magnitude higher for AQP4-M1 than for AQP4-M23 (Figure 5, B and C). In general, AQP4-M1 showed largely Brownian diffusion by RD analysis, whereas AQP4-M23 diffusion was highly restricted (Figure 5D). Diffusion of AQP4-M1 and AQP4-M23 in primary astrocyte cultures, which express high levels of endogenous AQP4, was nearly identical to those in COS-7 cells, as was AQP4-M1 and AQP4-M23 diffusion in primary astrocytes from AQP4 null mice that lack endogenous AQP4. To determine whether AQP4-M1 could integrate into AQP4-M23 arrays, we compared AQP4-M1 diffusion in control CHO-K1 cells to its diffusion in CHO cells that stably express high levels of nonepitope-tagged AQP4-M23 (CHO-M23 cells), which were shown previously by FFEM to contain a high density of OAPs (Yang *et al*., 1996). The presence of OAPs in the CHO-M23 cells reduced the average AQP4-M1 diffusion coefficient by ~26% ($p < 0.03$), but it did not create an increased confined population (as observed in Figure 3B) that would indicate a significant fraction incorporating in OAPs. Using the 95th percentile of AQP4-M23 range as the cutoff for OAP association, we found no change in the fraction (~9%) of AQP4-M1 below this range. The decrease in the diffusion coefficient of AQP4-M1 in the CHO-M23 cells is therefore likely due to membrane crowding effects, or weak transient interactions with the periphery of OAPs. AQP4-M1 diffusion was also slower in MDCK cells, a model of kidney epithelium, which is consistent with our previous studies of

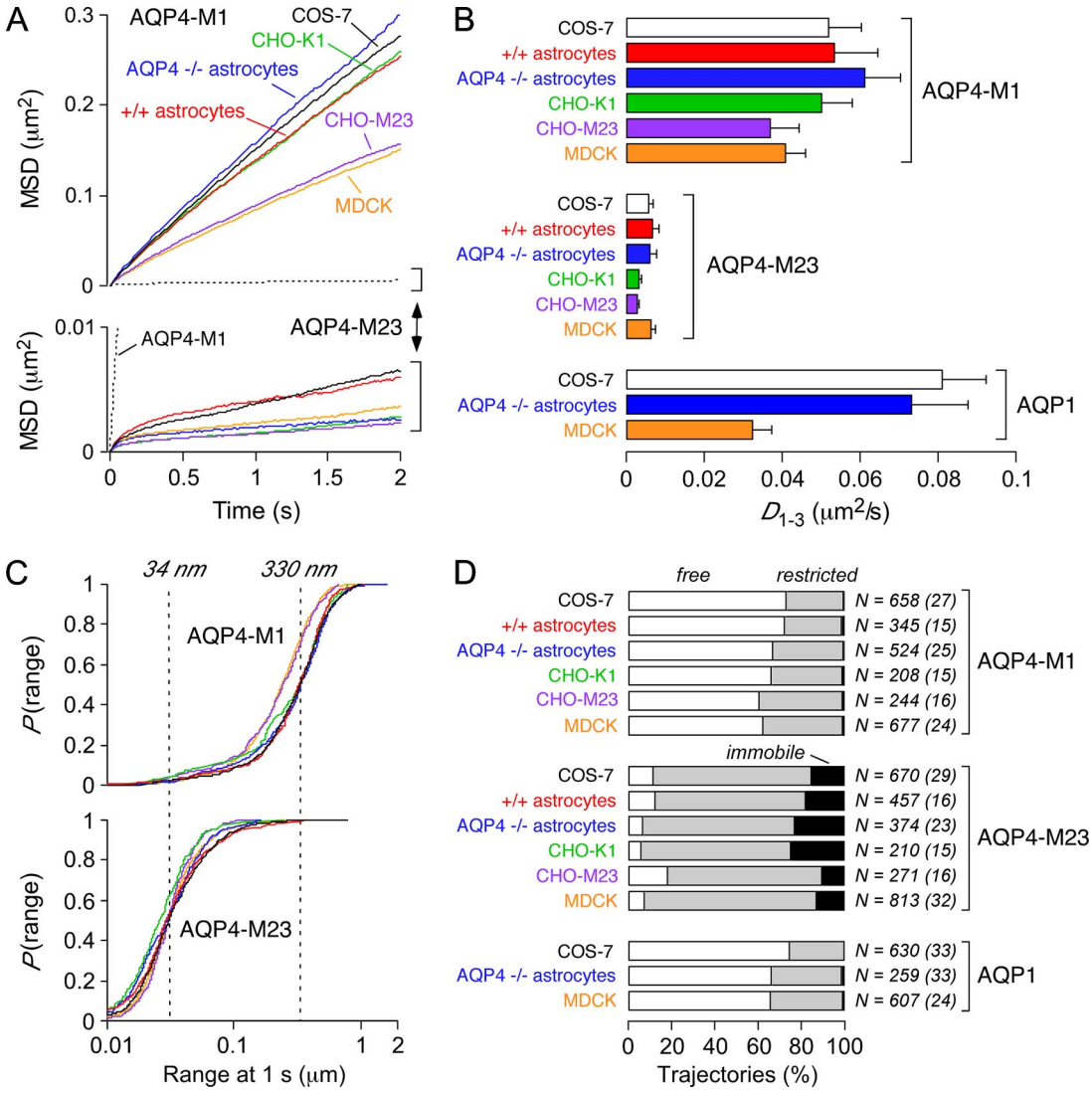

Figure 5. AQP4-M1 and AQP4-M23 diffusion in different cell types. (A) Combined MSD versus time plots for AQP4-M1 (top) and AQP4-M23 (bottom) in COS-7 cells (black), primary astrocyte cultures from wild-type mouse brain (red) or AQP4 null mouse brain (blue), CHO-K1 cells (green), M23-expressing CHO cells (CHO-M23, purple), and MDCK cells (orange). (B) Average diffusion coefficients of AQP4-M1 (top group), AQP4-M23 (middle group), and AQP1 (bottom group) in indicated cell types (colors same as in A) (mean ± SE). (C) Cumulative distribution of ranges at 1 s for AQP4-M1 (top) and AQP4-M23 (bottom) in different cells (colors as in A). Dashed lines indicate median ranges at 1 s of AQP4-M1 and AQP4-M23 in wild-type astrocytes. (D) Breakdown of diffusional modes as defined by RD analysis. *N* indicates the total number analyzed of trajectories, with the numbers of cells in parentheses.

AQP1 diffusion showing that MDCK cell membranes are more crowded than COS-7 cell membranes (Crane and Verkman, 2008).

Last, we developed a method to directly visualize the distribution of epitope-labeled AQP4 in membranes. To heavily label AQP4 molecules for TIRFM imaging, 100 times more primary and secondary antibody was used than in SPT experiments. In these studies, cells were fixed before labeling to prevent AQP4 clustering due to cross-linking that occurs when high concentrations of antibodies are used. In both COS-7 cells and primary astrocytes transfected with AQP4-M23, distinct puncta were visible, whereas AQP4-M1 and AQP1 seemed uniformly distributed in the membrane (Figure 6, A and B). Histograms of cluster pixel intensities, in which the unitary fluorescence F_0 of Alexa555-labeled secondary antibodies was determined from TIRFM images at very low labeling density (Figure 6C), estimated an average of ~136 secondary antibodies per cluster (Figure 6D). Similar average cluster fluorescence distributions were found for M23Δ6 in COS-7 cells (data not shown), suggesting similar OAP sizes. Analysis of FFEMs in the same cell line gave an average of 208 tetramers per OAP (assuming one tetramer per IMP), corresponding to ~800 AQP4 monomers per OAP. Comparing fluorescence images to FFEM, one Alexa555 secondary antibody was bound to approximately six c-myc sites, just under one binding event per AQP4 tetramer.

DISCUSSION

Single particle tracking of Qdots on AQP4 at an engineered external epitope was demonstrated to be a robust method for determining the array state of AQP4 in real time in live cells, and for investigating, for the first time, the membrane dynamics of free and OAP-associated AQP4. From image

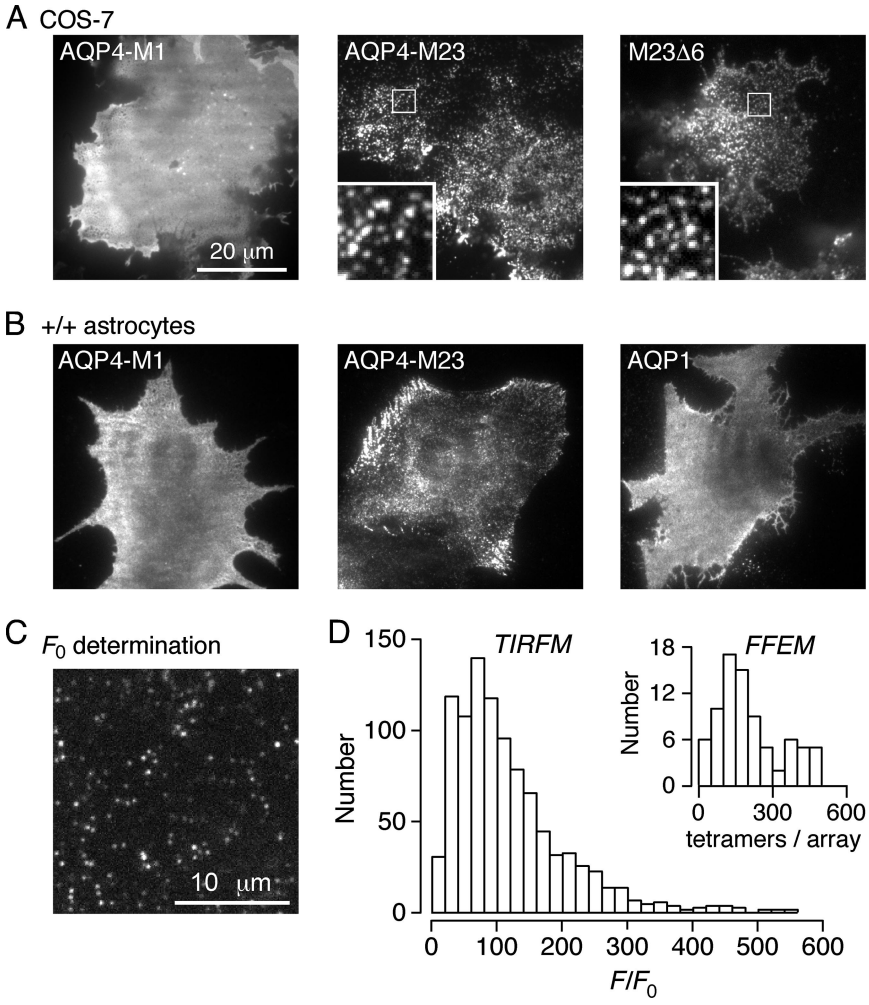

Figure 6. Visualization of AQP4 OAPs by total internal reflection fluorescence microscopy. TIRF micrographs of Alexa555-labeled AQP4-M1, AQP4-M23, and M23Δ6 in COS-7 cells (A) and AQP4-M1, AQP4-M23, and AQP1 in primary astrocyte cultures (B). Insets show expanded 5 × 5 μm areas. (C) TIRF micrograph of single Alexa555 secondary antibodies in AQP4-M1–expressing COS-7 cell labeled at very low density and imaged with 100-fold greater illumination intensity than in A and B. (D) Histogram of background-subtracted area-integrated fluorescence of Alexa555 clusters in six COS-7 cells expressing AQP4-M23. Cluster fluorescence normalized to that of a single Alexa555-labeled secondary antibody. Inset shows histogram of AQP4 tetramers per OAP from FFEM.

acquisition at rates up to 91 Hz over times up to 6 min, comparison of average diffusion coefficients and ranges clearly distinguished AQP4 isoforms that accumulate in arrays versus those that diffuse independently. By acquiring data at very different temporal resolutions, we were able to resolve the rapid, although highly confined diffusion of individual AQP4 molecules within OAPs from the slow diffusion of the OAPs themselves. A major advantage of SPT over methods that measure average diffusion, such as photobleaching, is the ability to examine the characteristics of individual molecules in large populations. Using the cumulative distribution of ranges at 1 s, we were able to detect and compare changes in populations of AQP4-M1 versus AQP4-M23, as well as detect mixed populations in cells coexpressing both isoforms. Also, using the positional density functions of AQP4 molecules exhibiting highly restricted diffusion, we were able to compute the energy potential function confining AQP4 within OAPs.

A central question in the AQP4 field concerns the role of the M1 isoform in modulating the assembly of AQP4-M23 in OAPs. Previous biochemical studies suggested that AQP4-M1 and AQP4-M23 exist as heterotetramers in vivo (Neely *et al*., 1999), and FFEM in cells cotransfected with both isoforms has shown relatively small OAPs compared with those in cells containing AQP4-M23 alone (Furman *et al*., 2003; Silberstein *et al*., 2004). We measured diffusion in COS-7 cells coexpressing AQP4-M1 and AQP4-M23 to determine whether AQP4-M1 would disrupt the formation of OAPs. The distribution of ranges at 1 s (Figure 3B) showed a bimodal population with diffusion coefficients of the confined and free fractions the same as that of pure AQP4-M23 and AQP4-M1, respectively. However, the range at 1 s for the OAP-associated subpopulation was increased compared with AQP4-M23 alone, suggesting that AQP4-M1 mildly disrupts packing in OAPs. Also, the average confining potential in the presence of AQP4-M1 was slightly lower than that of AQP4-M23 alone, with a significantly higher SD. These data are consistent with the findings from FFEM that OAPs are smaller in the presence of AQP4-M1. The potential due to intermolecular contacts in the OAP lattice is likely higher in the core than near the edge. The average measured potential therefore reflects the ratio of AQP4 molecules in the core of the OAP to those near the edge, producing a smaller average potential and a larger SD for smaller OAPs, as observed here. An alternative possibility is that small OAPs on the whole diffuse faster than large OAPs, such that the increased range found in the cotransfected cells is due to the combined effect of molecular and OAP diffusion. However, if the diffusion of small OAPs was significantly rapid to be detected by SPT at 91 Hz, an apparent increase in the diffusion coefficient would have been found, which was not.

To detect whether AQP4-M1 partitions into arrays we compared its diffusion in cells that expressed unlabeled AQP4 by using two systems: primary astrocyte cultures

from normal and AQP4 null mice and nontransfected and AQP4-M23-overexpressing CHO cells. AQP4-M1 diffusion was identical in wild-type and AQP4-deficient astrocytes, with no significantly confined fraction observed in either case. AQP4-M1 was only slightly slowed in the AQP4-M23–overexpressing CHO cells, consistent with increased membrane crowding or transient peripheral binding of AQP4-M1 to OAPs (Figure 5). Together, the data indicate that AQP4-M1 does not incorporate into OAPs; yet, the presence of AQP4-M1 in the membrane does affect the motions AQP4-M23 within OAPs, likely by reducing the overall size of OAPs. Therefore, in mixed systems of AQP4-M1 and AQP4-M23, the core of OAPs are composed entirely of AQP4-M23, whereas freely diffusing tetramers are likely a mixture of AQP4-M1 tetramers and heterotetramers. Near the edges of OAPs, a dynamic equilibrium exists between AQP4-M1 tetramers, AQP4-M23 tetramers, and heterotetramers. The competition for AQP4-M23 monomers near the edges of OAPs prevents them from growing to very large sizes. Further studies are needed to determine the details of this mechanism.

We used the spatial density profile of trajectories of confined AQP4-M23 diffusion to calculate the strength of the potential that acts on individual AQP4-M23 molecules in OAPs (Figure 4). The radial density profile fit well to a spring-like potential, but not other potential forms, with average spring constant of $\sim$6.5 pN/μm. The spring constant quantifies the molecular restoring force in response to particle displacement from its minimum energy position on OAP lattice points. We had expected that AQP4 confinement in OAPs might resemble that of a rigid corral, giving rise to a hard-wall potential (Saxton, 1995). The spring-like potential found here indicates that the interior of the array is mildly flexible, although the spring constant confining AQP4-M23 was nearly threefold greater than that confining a different protein, CFTR, which is tethered to the actin skeleton by PDZ interactions (Haggie *et al*., 2006; Jin *et al*., 2007). The potential confining AQP4-M23 was not altered significantly by preventing cytoskeletal or PDZ interactions, indicating, as hypothesized, that the potential is determined by interactions with adjacent AQP4 molecules in OAPs.

Deletion of the C-terminal PDZ binding domain of AQP4-M23 did not change its short-time diffusion coefficient, range distribution, or spring constant, indicating that AQP4 array formation and stability is independent of PDZ interactions (Figures 3 and 4). We also found that M1Δ6 diffused over seconds only slightly faster and further than AQP4-M1 (Figure 3). These data suggest that AQP4 C-terminal PDZ interactions are weak compared with the OAP-forming interactions. However, time-lapse SPT over minutes showed that M23Δ6 OAPs diffused over a approximately twofold greater range than AQP4-M23 OAPs (Figure 2). Therefore, PDZ interactions are strong enough to overcome the very slow diffusion of large OAPs, and anchor OAPs to relatively immobile structures below the plasma membrane. Treatments with latrunculin or nocodazole to depolymerize actin or tubulin, respectively, had little effect on the diffusion of OAPs compared with the effect of the truncation mutation, indicating that the anchoring of AQP4 OAPs does not involve direct interaction with cytoskeletal elements. Stabilization of actin filaments by jasplakinolide slightly reduced the diffusion of OAPs, but did not change the confining potential on AQP-M23 within arrays or inhibit AQP4-M1 diffusion. The effect of jasplakinolide is probably due to a secondary interaction between actin and OAPs, perhaps by altering mobility of other membrane proteins, rather than to a direct interaction with AQP4.

A surprising finding revealed by time-lapse SPT was that the MSDs of OAPs exhibited a slightly upward curvature with time (Figure 2D). Upward curvature of an MSD plot could arise from diffusion superimposed on directed transport along intracellular elements or bulk flow (Saxton, 1994). Disruption of cytoskeletal elements or deletion of PDZ interactions did not eliminate the upward curvature, so that directed transport of OAPs, if it occurs, does not involve actin filaments or microtubules, nor does it require PDZ-mediated interactions. We propose that convective bulk flow of membrane patches would mildly propel OAPs in the plasma membrane, such that AQP4 molecules would move further at long times than from simple diffusion (producing upward curved MSD plots). This proposed convective flow would be too slow to be seen in rapidly diffusing individual proteins and/or lipids, and it would not be seen for cytoskeleton-anchored proteins, but it would be visible for large rigid structures such as OAPs that diffuse very slowly. Further studies are needed to prove the existence of the slow convective membrane flow suggested by our experiments.

Our data are consistent with a recent model in which AQP4 in OAPs in astrocyte membranes is anchored by PDZ interactions with α-syntrophin and/or dystrophin (for review, see Amiry-Moghaddam *et al*., 2004). This model was based on the finding that α-syntrophin deletion results in a loss of perivascular accumulation of AQP4 in astrocytes (Neely *et al*., 2001). It has also been suggested that AQP4 anchoring to α-syntrophin may lead to coupling of AQP4 to K^+ channel Kir4.1 (Nagelhus *et al*., 2004); however, recent results from our laboratory provide evidence against a functional link between AQP4 and Kir4.1 (Zhang and Verkman, 2008). Based on our direct evidence that AQP4 in OAPs is anchored by PDZ interactions on the cytoplasmic side of the membrane, we propose that assembly of AQP4 in OAPs allows a large number of AQP4 molecules to remain nearly fixed at specific locations with a minimal number of anchoring points. High densities of AQP4 at specific locations may be important for localized, high water permeability in astrocyte foot processes at the blood-brain barrier, or perhaps for astrocyte cell–cell adhesion.

In summary, we used SPT of Qdot-labeled AQP4 to characterize OAPs in live cells. Using the dynamic information provided by diffusion data, we conclude that AQP4 is solely responsible for OAP formation and stability, independently of cytoskeletal or PDZ-mediated interactions. AQP4-M1 does not incorporate in OAPs, but it modulates array size by competing for AQP4-M23 monomers at the OAP edges. AQP4-M23 is highly confined within OAPs in a springlike potential, although OAPs on the whole diffuse very slowly in the plasma membrane. Finally, we provide evidence for an intermolecular interaction, mediated by the C-terminal PDZ binding domain of AQP4, which anchors OAPs to unknown structures on the cytoplasmic side of the membrane. The anchoring interaction significantly reduces long-range motions of AQP4-M23 due to OAP diffusion and/or bulk membrane flow, supporting the conclusion that PDZ interactions and OAP formation are critical for AQP4 polarization in specific membrane domains.

ACKNOWLEDGMENTS

We thank Dr. Hua Zhang for providing primary astrocyte cell cultures and Dr. Andrew Bullen of the University of California San Francisco/Nikon Biological Imaging Development Center for confocal microscopy. This work was supported by National Institutes of Health grants DK-35124, EB-00415, HL-73856, HL-59198, EY-13574, and DK-72517, and Research Development Program and Drug Discovery grants from the Cystic Fibrosis Foundation. Dr.

Crane was supported in part by National Institutes of Health National Research Service Award GM-808512.

REFERENCES

Amiry-Moghaddam, M., Frydenlund, D. S., and Ottersen, O. P. (2004). Anchoring of aquaporin-4 in brain: molecular mechanisms and implications for the physiology and pathophysiology of water transport. Neuroscience *129*, 999–1010.

Crane, J. M., and Verkman, A. S. (2008). Long-range nonanomalous diffusion of quantum dot-labeled aquaporin-1 water channels in the cell plasma membrane. Biophys. J. *94*, 702–713.

Evan, G., Lewis, G., Ramsay, G., and Bishop, J. (1985). Isolation of monoclonal antibodies specific for human c-myc proto-oncogene product. Mol. Cell. Biol. *5*, 3610–3616.

Frigeri, A., Gropper, M. A., Umenishi, F., Kawashima, M., Brown, D., and Verkman, A. S. (1995). Localization of MIWC and GLIP water channel homologs in neuromuscular, epithelial and glandular tissues. J. Cell Sci. *108*, 2993–3002.

Fujiwara, T., Ritchie, K., Murakoshi, H., Jacobson, K., and Kusumi, A. (2002). Phospholipids undergo hop diffusion in compartmentalized cell membrane. J. Cell Biol. *157*, 1071–1081.

Furman, C. S., Gorelick-Feldman, D. A., Davidson, K. G., Yasumura, T., Neely, J. D., Agre, P., and Rash, J. E. (2003). Aquaporin-4 square array assembly: opposing actions of M1 and M23 isoforms. Proc. Natl. Acad. Sci. USA *100*, 13609–13614.

Haggie, P., Kim, J., Lukacs, G., and Verkman, A. S. (2006). Tracking of quantum dot-labeled CFTR shows near immobilization by C-terminal PDZ interactions. Mol. Biol. Cell *17*, 4937–4945.

Hasegawa, H., Ma, T., Skach, W., Matthay, M. A., and Verkman, A. S. (1994). Molecular cloning of a mercurial-insensitive water channel expressed in selected water-transporting tissues. J. Biol. Chem. *269*, 5497–5500.

Hatton, J. D., and Ellisman, M. H. (1982). The distribution of orthogonal arrays in the freeze-fractured rat median eminence. J. Neurocytol. *11*, 335–349.

Hatton, J. D., and Ellisman, M. H. (1984). Orthogonal arrays are redistributed in the membranes of astroglia from alumina-induced epileptic foci. Epilepsia *25*, 145–151.

Hiroaki, Y. *et al*. (2006). Implications of the aquaporin-4 structure on array formation and cell adhesion. J. Mol. Biol. *355*, 628–639.

Jin, S., Haggie, P., and Verkman, A. S. (2007). Single-particle tracking of membrane protein diffusion in a potential: simulation, detection, and application to confined diffusion of CFTR Cl^- channels. Biophys. J. *93*, 1079–1088.

Jung, J. S., Bhat, R. V., Preston, G. M., Guggino, W. B., Baraban, J. M., and Agre, P. (1994). Molecular characterization of an aquaporin cDNA from brain: candidate osmoreceptor and regulator of water balance. Proc. Natl. Acad. Sci. USA *91*, 13052–13056.

Kusumi, A., Sako, Y., and Yamamoto, M. (1993). Confined lateral diffusion of membrane receptors as studied by single particle tracking (nanovid microscopy). Effects of calcium-induced differentiation in cultured epithelial cells. Biophys. J. *65*, 2021–2040.

Landis, D. M., and Reese, T. S. (1974). Arrays of particles in freeze-fractured astrocytic membranes. J. Cell Biol. *60*, 316–320.

Lu, M., Lee, M. D., Smith, B. L., Jung, J. S., Agre, P., Verdijk, M. A., Merkx, G., Rijss, J. P., and Deen, P. M. (1996). The human AQP4 gene: definition of the locus encoding two water channel polypeptides in brain. Proc. Natl. Acad. Sci. USA *93*, 10908–10912.

Lu, Y., Turnbull, I. R., Bragin, A., Carveth, K., Verkman, A. S., and Skach, W. R. (2000). Reorientation of aquaporin-1 topology during maturation in the endoplasmic reticulum. Mol. Biol. Cell *11*, 2973–2985.

Ma, T., Yang, B., Gillespie, A., Carlson, E. J., Epstein, C. J., and Verkman, A. S. (1997). Generation and phenotype of a transgenic knockout mouse lacking the mercurial-insensitive water channel aquaporin-4. J. Clin. Invest. *100*, 957–962.

Nagelhus, E. A., Mathiisen, T. M., and Ottersen, O. P. (2004). Aquaporin-4 in the central nervous system: cellular and subcellular distribution and coexpression with Kir4.1. Neuroscience *129*, 905–913.

Neely, J. D., Amiry-Moghaddam, M., Ottersen, O. P., Froehner, S. C., Agre, P., and Adams, M. E. (2001). Syntrophin-dependent expression and localization of Aquaporin-4 water channel protein. Proc. Natl. Acad. Sci. USA *98*, 14108–14113.

Neely, J. D., Christensen, B. M., Nielsen, S., and Agre, P. (1999). Heterotetrameric composition of aquaporin-4 water channels. Biochemistry *38*, 11156–11163.

Rash, J. E., Staehelin, L. A., and Ellisman, M. H. (1974). Rectangular arrays of particles on freeze-cleaved plasma membranes are not gap junctions. Exp. Cell Res. *86*, 187–190.

Rash, J. E., Yasumura, T., Hudson, C. S., Agre, P., and Nielsen, S. (1998). Direct immunogold labeling of aquaporin-4 in square arrays of astrocyte and ependymocyte plasma membranes in rat brain and spinal cord. Proc. Natl. Acad. Sci. USA *95*, 11981–11986.

Saadoun, S., Papadopoulos, M. C., Watanabe, H., Yan, D., Manley, G. T., and Verkman, A. S. (2005). Involvement of aquaporin-4 in astroglial cell migration and glial scar formation. J. Cell Sci. *118*, 5691–5698.

Saxton, M. (1997). Single-particle tracking: the distribution of diffusion coefficients. Biophys. J. *72*, 1744–1753.

Saxton, M. J. (1994). Single-particle tracking: models of directed transport. Biophys. J. *67*, 2110–2119.

Saxton, M. J. (1995). Single-particle tracking: effects of corrals. Biophys. J. *69*, 389–398.

Schotland, D. L., Bonilla, E., and Wakayama, Y. (1981). Freeze fracture studies of muscle plasma membrane in human muscular dystrophy. Acta Neuropathol. *54*, 189–197.

Shi, L. B., Skach, W. R., Ma, T., and Verkman, A. S. (1995). Distinct biogenesis mechanisms for the water channels MIWC and CHIP28 at the endoplasmic reticulum. Biochemistry *34*, 8250–8256.

Silberstein, C., Bouley, R., Huang, Y., Fang, P., Pastor-Soler, N., Brown, D., and Van Hoek, A. N. (2004). Membrane organization and function of M1 and M23 isoforms of aquaporin-4 in epithelial cells. Am. J. Physiol. Renal Physiol. *287*, F501–F511.

Solenov, E., Watanabe, H., Manley, G. T., and Verkman, A. S. (2004). Sevenfold-reduced osmotic water permeability in primary astrocyte cultures from AQP-4-deficient mice, measured by a fluorescence quenching method. Am. J. Physiol. Cell Physiol. *286*, C426–C432.

Van Hoek, A. N., Ma, T., Yang, B., Verkman, A. S., and Brown, D. (2000). Aquaporin-4 is expressed in basolateral membranes of proximal tubule S3 segments in mouse kidney. Am. J. Physiol. Renal Physiol. *278*, F310–F316.

Verbavatz, J. M., Ma, T., Gobin, R., and Verkman, A. S. (1997). Absence of orthogonal arrays in kidney, brain and muscle from transgenic knockout mice lacking water channel aquaporin-4. J. Cell Sci. *110*, 2855–2860.

Verkman, A. S., Binder, D. K., Bloch, O., Auguste, K., and Papadopoulos, M. C. (2006). Three distinct roles of aquaporin-4 in brain function revealed by knockout mice. Biochim. Biophys. Acta *1758*, 1085–1093.

Yang, B., Brown, D., and Verkman, A. S. (1996). The mercurial insensitive water channel (AQP-4) forms orthogonal arrays in stably transfected Chinese hamster ovary cells. J. Biol. Chem. *271*, 4577–4580.

Yang, B., Ma, T., and Verkman, A. (1995). cDNA cloning, gene organization, and chromosomal localization of a human mercurial insensitive water channel. Evidence for distinct transcriptional units. J. Biol. Chem. *270*, 22907–22913.

Yang, B., Van Hoek, A. N., and Verkman, A. S. (1997). Very high single channel water permeability of aquaporin-4 in baculovirus-infected insect cells and liposomes reconstituted with purified aquaporin-4. Biochemistry *36*, 7625–7632.

Zhang, H., and Verkman, A. S. (2008). Aquaporin-4 independent Kir4.1 K^+ channel function in brain glial cells. Mol. Cell. Neurosci. *37*, 1–10.